Engineering Structures 291 (2023) 116435

Contents lists available at ScienceDirect

Engineering Structures

journal homepage: www.elsevier.com/locate/engstruct

An integrated method of topological optimization and path design for 3D concrete printing

Wenwei Yang [a], Li Wang [a,b,*], Guowei Ma [a,b,*], Peng Feng [c]

[a] School of Civil and Transportation Engineering, Hebei University of Technology, 5340 Xiping Road, Beichen District, Tianjin 300401, China
[b] Tianjin Key Laboratory of Prefabricated Building and Intelligent Construction, Hebei University of Technology, 5340 Xiping Road, Beichen District, Tianjin 300401, China
[c] MOE Key Lab of Civil Engineering Safety and Durability, Department of Civil Engineering, Tsinghua University, Beijing 100084, China

A R T I C L E I N F O

Keywords:
3D concrete printing
Topology optimization
Path planning
Integration of design and manufacturing
High performance structure

A B S T R A C T

As an advanced construction technology, 3D concrete printing (3DCP) has the advantage of high manufacturing freedom for various freeform structures. The digital design of 3D printing using topology optimization contributes to obtaining the maximum performance potential from manufactured structures. However, most digitally designed structures obtained by topology optimization cannot be directly manufactured using 3DCP owing to various manufacturing constraints that have not yet been considered in the design process. This paper presents an integrated design method for 3DCP by incorporating extrusion-based manufacturing characteristics into the topology optimization algorithm. Topological optimization is based on the solid isotropic material with penalization (SIMP) method owing to its ease of adaptation to multiple constraints. During the optimization iteration, the manufacturing characteristics of nozzle size and path continuity are considered as the design requirements of 3D printed structures to achieve high-quality manufacturing by using intermittent interruption of topology optimization to modify the design variables. Meanwhile, the anisotropic behaviors of material constraints and the volume and Tsai-Wu criterion of design constraints are introduced to obtain the desired mechanical performance with lightweight designs. Moreover, the number of closed regions and overhang angle controls are incorporated to ensure the global path continuity and stable stacking of optimized 3D structures. A concrete arch structure is 3D printed to validate the proposed integrated method, and the removal of breakpoints and short paths and complete filling rate are demonstrated. The integrated method facilitates the engineering application of 3DCP in a high-efficiency and high-quality manner.

1. Introduction

3D concrete printing (3DCP), as a layer-by-layer deposition process, has the advantage of high manufacturing freedom for various freeform structures [1,2]. The promising manufacturing advantages of 3DCP for structural construction are validated by constructing various architectural and civil structures, such as houses, bridges, and bus stations [3,4]. Meanwhile, new cementitious composite materials and reinforcement strategies compatible with 3DCP have been diversified and explored [5–7], which are related to the mechanical characteristics of printed concrete structures [8,9]. The structural performances of 3D printed structures still require further optimization to fully exploit the advantages of 3DCP in material distribution.

Topology optimization is an advanced design approach for obtaining high-performance structures, which has been successfully applied to the lightweight design of structures in the engineering field [10–13]. The design structures obtained by topology optimization are difficult to print owing to the lack of integration with manufacturing constraints during the design process. The 3D printed concrete permanent formwork method and hybrid fabrication using additive and subtractive manufacturing technologies have been explored for the manufacturing of topologically optimized structures [14,15]. These methods have unique advantages that can be exploited during a construction process following optimal design. However, the fabrication processes still require extra treatment or manual operation, and therefore, the flexibility and efficiency are reduced.

For fused deposition modeling (FDM) and metal additive manufacturing, certain manufacturing constraints have been explored

* Corresponding authors.
E-mail addresses: wangl1@hebut.edu.cn (L. Wang), guowei.ma@hebut.edu.cn (G. Ma).

https://doi.org/10.1016/j.engstruct.2023.116435

Available online 15 June 2023

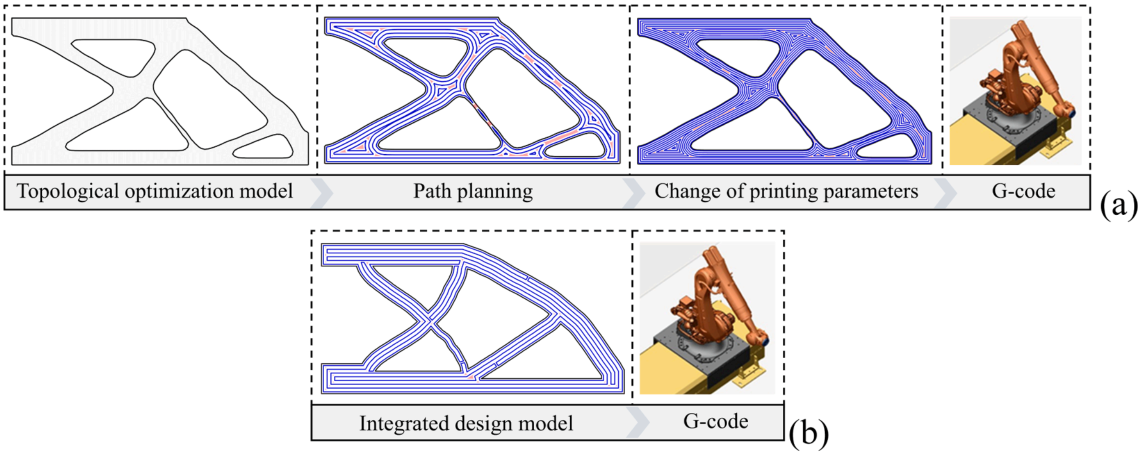

Fig. 1. Design process of G-code for 3D printing through (a) traditional separated design and (b) integrated design.

regarding the topology optimization, such as minimum size, overhang, connectivity, tool path continuity, and distortion constraints [16–20]. However, the 3D concrete printing process retains its unique manufacturing characteristics, such as nozzle size and path continuity, which are different from those of polymer and metal manufacturing. Thus, the available practices cannot be directly applied to 3DCP. An integrated design between 3DCP and topology optimization needs further research attention.

It is crucial to effectively combine the digital design of topology optimization and the 3DCP technique to realize the maximum performance potential of manufactured structures. The post-tensioned concrete girder constructed by Ghent University achieved 20 % material savings, as well as an effective combination of topology optimization and 3DCP. This was the first demonstration of how topological design combined with 3DCP could allow for creating efficient structures using less material [21]. The integrated design considering the manufacturing constraints of 3DCP enhances the manufacturability of the optimized structures without post-processing. Although Carstensen [22] and Fernández et al. [23] successfully considered the nozzle size constraint of 3DCP, the anisotropy, path-continuity constraint, and overhang angle constraint, which are highly relevant for material extrusion-type additive manufacturing, have not been considered. In particular, breakpoints are unfavorable for 3DCP, and multiple startups and shutdowns will lead to unstable extruded materials or worse printing quality. Moreover, the removal of supporting materials is very difficult, which can easily cause structural damage. Pastore et al. [24] proposed a Bézier-based biased random-key genetic algorithm that addressed only the nozzle size and path-continuity constraints. Bi et al. [25] addressed various manufacturing constraints of 3DCP. However, there exist many short zigzag paths causing to accumulate concrete materials because the nozzle size constraint is not considered. Previous optimization methods address only a few problems of manufacturing constraints for 3DCP and still face various challenges. Anisotropy has not been fully utilized, and path planning is based on optimized geometric shapes and cannot achieve collaborative optimization in the design process.

In this study, an integrated method regarding structural design and manufacturing for 3D printed concrete structures is proposed by incorporating the manufacturing parameters of 3DCP into the design processes of topology optimization. Both the manufacturing constraints, for example, nozzle size, path continuity, and overhang angle, and mechanical performance constraints, for example, modulus anisotropy and stress constraint, are considered. Global path continuity and high printing quality are demonstrated via designing and 3D printing a concrete assembled arch structure. Subsequently, the applicability of the proposed integrated method is validated.

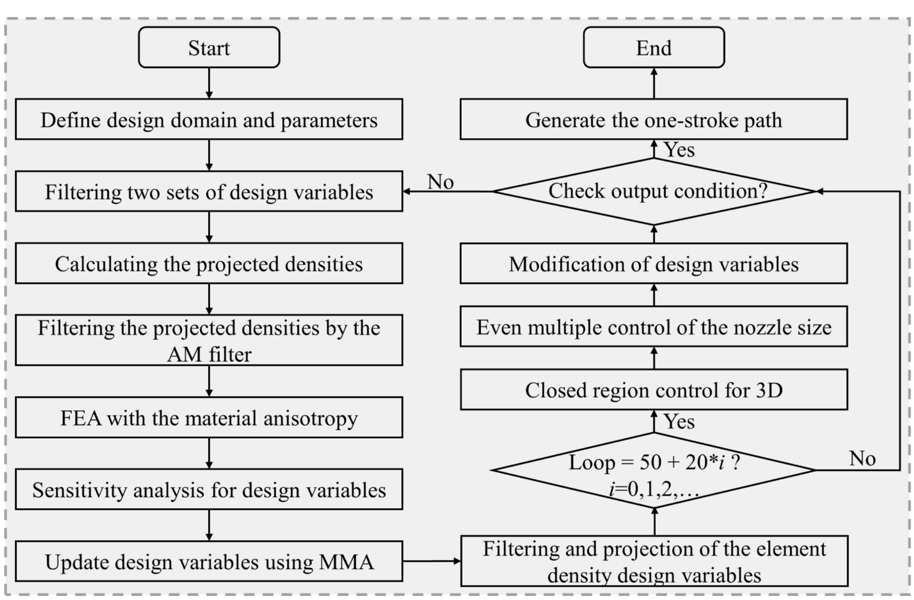

Fig. 2. The flowchart of the proposed integration design.

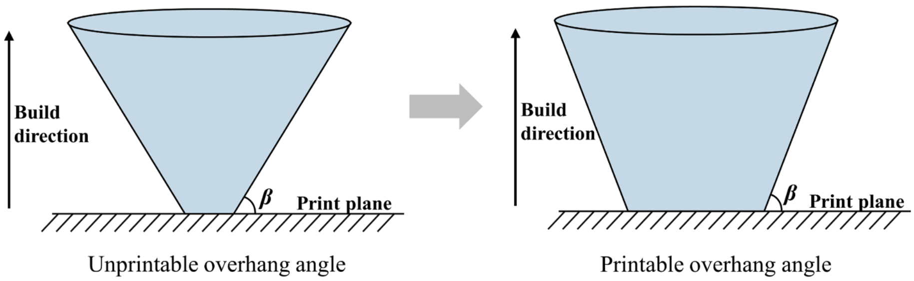

Fig. 3. Schematic of the overhang angle control for 3D structures.

2. Integrated design method for 3DCP

The integrated structural design method for 3D printed concrete structures is based on a conventional topology optimization method that incorporates various manufacturing constraints of 3DCP. The addition of manufacturing constraints can directly obtain an optimized pattern with respect to the printing path, and the filling rate and printing quality can be ensured effectively. In the conventional approaches, the topology and path are designed separately and require further modification. Accordingly, the final results of the G-code are not of high quality owing to the mismatch between design and manufacturing, as shown in Fig. 1(a). The proposed method can generate an optimized G-code file based on the one-stroke printing path directly without extra updates and modifications (Fig. 1(b)).

2.1. Topological optimization design based on SIMP method

The proposed integrated design method adopts the filtering and projection methods and modifies the design variables in certain iteration steps to obtain an optimization result with the high fill rate and one-stroke printing path. The flowchart of the proposed integrated design method is shown in Fig. 2. The optimization starts from the definition of the design domain and parameters, such as load, support, finite element analysis (FEA) mesh, material parameters, solving parameters, etc. The design variables are filtered and projected to avoid numerical instability problems and obtain a black-and-white solution. The additive manufacturing (AM) filter is integrated in the optimization process to achieve the overhang angle control for 3D structures that is difficult to be avoided for the conventional 3D structural optimization design. After completing the above steps, the FEA considering the material anisotropic constraints is carried out for calculating sensitivity values and to update the design variables. The filtering and projection methods shall be performed when the updated design variables do not satisfy the overhang angle control.

To reduce the computation time while providing sufficient optimization steps for structural optimization, the closed region and even multiple control for structures are introduced at the 50$^{\text{th}}$ iteration and then introduced every 20 iterations to satisfy the nozzle size and path-continuity controls. The closed region control is applied before the even multiple control to provide the useful skeleton form for the nozzle size control. Then, the design variables are modified to guarantee the printing quality of optimized structures and the optimized result is checked whether meeting the output condition. If the number of iterations is not equal to 50 + 20i, check the output condition directly. The optimization is looped and terminated until meeting the output condition. When the optimization results meet the following three conditions, they can be output: (1) the volume and stress constraints are satisfied; (2) the force transmission path of the structure before and after applying the manufacturing constraint is the same, that is, the number corresponding to the central axis is the same; and (3) the structure has clear boundaries and few gray elements. Note that the volume constraint may not strictly meet the requirements; therefore, the results can be output without satisfying this specific requirement. The generation of the one-stroke path is performed at the end of the optimization to avoid that the stress concentration of the interruption and reconnection areas affect the accuracy of optimization results and the optimization iteration terminates.

The objective of structural design is to minimize structural compliance by considering material volume, stress, and manufacturing as constraints. The material volume and stress constraints are explicit, and the overhang angle is controlled by the AM filter. The nozzle size and path-continuity controls of manufacturing constraints are achieved by modifying the design variables at some number of iterations during the optimization process. To make full use of the anisotropy, the design variable of the printing angle is added based on the solid isotropic material with penalization (SIMP) method [26]. The proposed topology optimization problem can be formulated as:

$$\begin{aligned} \text{find } \boldsymbol{\rho} &= \{\rho_1,\rho_2,\dots\dots,\rho_{\text{n}}\}^{\text{T}}, \boldsymbol{\theta} = \{\theta_1,\theta_2,\dots\dots,\theta_{\text{n}}\}^{\text{T}} \\ \min \mathrm{C}(\boldsymbol{\rho},\boldsymbol{\theta}) &= \mathbf{U}(\boldsymbol{\rho},\boldsymbol{\theta})^{\text{T}}\mathbf{K}(\boldsymbol{\rho},\boldsymbol{\theta})\mathbf{U}(\boldsymbol{\rho},\boldsymbol{\theta}) \\ V &= \sum_{e=1}^{n}\rho_e v_e \leqslant f V_0 \\ & g_{\max}(\boldsymbol{\rho},\boldsymbol{\theta}) \leqslant 1 \\ & \rho_{\min} \leqslant \rho_e \leqslant 1 \\ & -\pi \leqslant \theta_e \leqslant \pi, e = 1,2,\dots,n \end{aligned}$$

where $\boldsymbol{\rho}$ and $\boldsymbol{\theta}$ are the design variables, namely, element density and printing angle vectors, respectively; n is the number of elements used to discretize the design domain; C is the structural compliance; ρ_e and v_e are the density and volume of the e^{th} element, respectively; $\boldsymbol{K}$ and $\boldsymbol{U}$ are the global stiffness matrix and nodal displacement vectors, respectively; V and V_0 are the material and design domain volumes, respectively; f is the prescribed volume fraction. The Tsai-Wu criterion for stress constraint is selected owing to anisotropy accordingly. $g_{\max}$ is the maximum Tsai-Wu value in the design domain. $\rho_{\min}$ is the minimum allowable element density, which is a non-zero value to avoid singularity and is set as 10^{-8} conventionally.

To avoid numerical instability problems such as checkerboard and ensure the fiber continuity, design variables are filtered by computing the weighted average of design variables in set N_e for each element. The filtered design variables are expressed as [27]:

$$\overline{\rho}_e = \frac{\sum_{i\in N_e}\rho_i w(\mathbf{x}_i - \overline{\mathbf{x}}^e)}{\sum_{i\in N_e} w(\mathbf{x}_i - \overline{\mathbf{x}}^e)}, \overline{\theta}_e = \frac{\sum_{i\in N_e}\theta_i w(\mathbf{x}_i - \overline{\mathbf{x}}^e)}{\sum_{i\in N_e} w(\mathbf{x}_i - \overline{\mathbf{x}}^e)} \tag{2}$$

where N_e is the set of elements in the domain of influence of element e; $\mathbf{x}_i$ is the position of element i; $w(\mathbf{x}_i - \overline{\mathbf{x}}^e)$ is a weight factor defined as:

$$w(\mathbf{x}_i - \overline{\mathbf{x}}^e) = \begin{cases} r_{\min} - ||\mathbf{x}_i - \overline{\mathbf{x}}|| & \text{if } \mathbf{x}_i \in N_e \\ 0 & \text{otherwise} \end{cases} \tag{3}$$

where $||\mathbf{x}_i - \overline{\mathbf{x}}^e||$ is the distance between the centers of the element e and element i; $r_{\min}$ is the filter radius.

Applying the filter of density design variables leads to gray transition regions with intermediate densities between 0 and 1, and the threshold projection based on the tanh function is adopted to constrain the elemental design variables to reach 0 or 1 [28,29]. The projected density

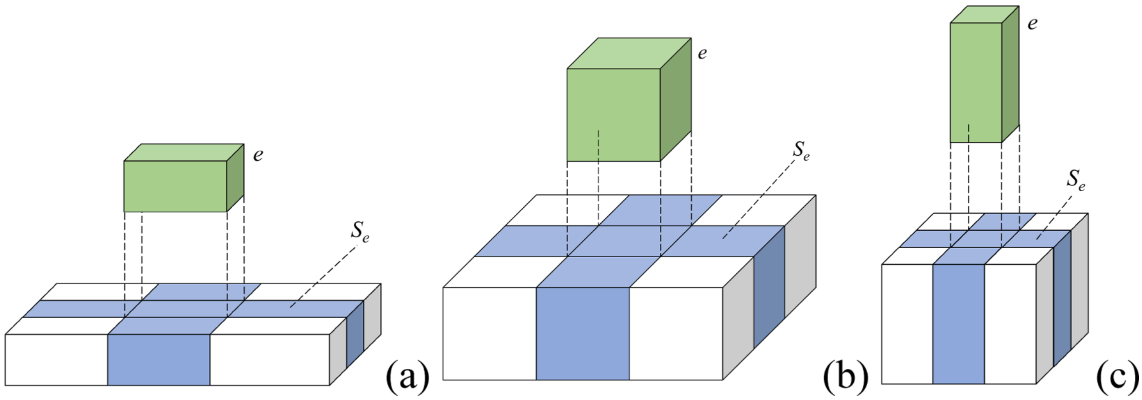

Fig. 4. Definition of the AM filter with overhang angles of (a) 26.6°, (b) 45° and (c) 63.4°.

can be written as:

$$\widetilde{\rho}_e = \frac{\tanh(\beta\eta) + \tanh(\beta(\overline{\rho}_e - \eta))}{\tanh(\beta\eta) + \tanh(\beta(1-\eta))} \tag{4}$$

where β is the curvature of the regularization that approaches the Heaviside function as β approaches infinity. A continuation method is used such that β is initially chosen to be small and is raised in subsequent iterations to achieve a near 0–1 topology. Here, β is initialized at 1.0 and is increased by 1 if a change in the objective function has reached the set value, and the maximum value is 50. η is the threshold for controlling the projection, which is set to 0.5.

For 2D structural optimization, since the print plane is determined in advance, the printed component is only the stretching of the 2D structure and does not involve the control of the overhang angle. For 3D structure optimization, the overhang angle control should be satisfied along the stacking direction to avoid components from being unprintable or collapsing during printing owing to high overhang angles, as shown in Fig. 3.

The overhang angle control is applied to the optimization process in the form of an AM filter [16] such that each printed density cannot be higher than the maximum printed density in its supporting region, which is expressed as follows:

$$\widehat{\widetilde{\rho}}_e = \min\left(\widetilde{\rho}_e, \widehat{\widetilde{\rho}}_e^S\right), \widehat{\widetilde{\rho}}_e^S = \max_{i \in S_e} \widehat{\widetilde{\rho}}_i \tag{5}$$

where $\widehat{\widetilde{\rho}}_e$ is the printed density, $\widehat{\widetilde{\rho}}_e^S$ is the maximum printed density in the supporting region S_e, and $\widetilde{\rho}_e$ is a blueprint density variable, which is the projected density.

In Fig. 4, the blue region S_e denotes the supporting region of an element e. When the printing material is not printed in this supporting region, the structure cannot be printed. Different overhang angles can be satisfied by changing the aspect ratio of the elements. Fig. 4(a–c) show different overhang angles of 26.6°, 45°, and 63.4°, respectively. A more detailed representation can be found in a previous study [16].

Anisotropy is mainly reflected when calculating the rotated elastic matrix $\boldsymbol{D}_e$, which is expressed as follows:

$$\boldsymbol{D}_e = \boldsymbol{T}(\theta)\boldsymbol{D}_0\boldsymbol{T}(\theta)^{-1} \tag{6}$$

where θ is the rotation angle, $\boldsymbol{T}$ is the rotation matrix, and $\boldsymbol{D}_0$ is the initial elastic matrix before rotation, which corresponds to the orthogonal anisotropic elastic matrix in the 2D model and transverse isotropic elastic matrix in the 3D model.

The Tsai–Wu failure criterion is adopted for the stress constraint owing to the anisotropy. The calculation formula of the Tsai-Wu value in the 2D and 3D models can be expressed as follows:

$$g_e = F_1\sigma_1 + F_2\sigma_2 + F_{11}\sigma_1^2 + F_{22}\sigma_2^2 + 2F_{12}\sigma_1\sigma_2 + F_{66}\tau_{12}^2 \tag{7}$$

$$g_e = F_{11}\sigma_1^2 + F_{22}\left(\sigma_2^2 + \sigma_3^2\right) + (2F_{22} - F_{44})\sigma_2\sigma_3 + 2F_{12}\sigma_1(\sigma_2 + \sigma_3) + F_1\sigma_1 + F_2(\sigma_2 + \sigma_3) + F_{44}\tau_{23}^2 + F_{66}\left(\tau_{21}^2 + \tau_{31}^2\right) \tag{8}$$

where the coefficients F_i and F_{ij} can be obtained in terms of compressive strengths X_c and Y_c, tensile strengths X_t and Y_t, and longitudinal and transverse shear strengths S_{12} and S_{23}, respectively. Details regarding the parameter calculation can be found in the literature [30,31].

The sensitivity for the objective and constraint functions with respect to the design variables can be calculated by the chain rule. The readers are referred to the publications for more detailed [32]. Because the optimization proposed in this paper is a design problem with multiple design variables and multiple constraints. The method of moving asymptotes (MMA) is selected to solve the optimization problem [33].

2.2. Adaptive nozzle size control of 3DCP

The adaptive nozzle size control of structural features is achieved through the medial axis transform (MAT), which has been applied to precisely control the minimum/maximum length scale [34–38]. As shown in Fig. 5, the incorporation of the adaptive nozzle size control into topology optimization involves boundary extraction, medial axis extraction, width selection, path planning, and modification of design variables.

(1) Boundary fitting.

A contour plotting algorithm is first deployed to obtain the geometry boundary, which is the foundation for obtaining the medial axis. If the contour plotting is performed directly, the structural boundaries may appear jagged, which is not conducive to the extraction of the medial axis. Therefore, curve fitting is performed to obtain smooth boundaries and a B-spline curve of order p [39] is used. In this study, a B-spline curve of order 3 is considered.

(2) Medial axis extraction based on MAT.

After obtaining the structural boundaries, the main force transmission path of the structure is obtained by extracting the medial axis. The medial axis extraction process is illustrated in Fig. 6. First, a constrained Delaunay triangulation of a sample of points collected on the

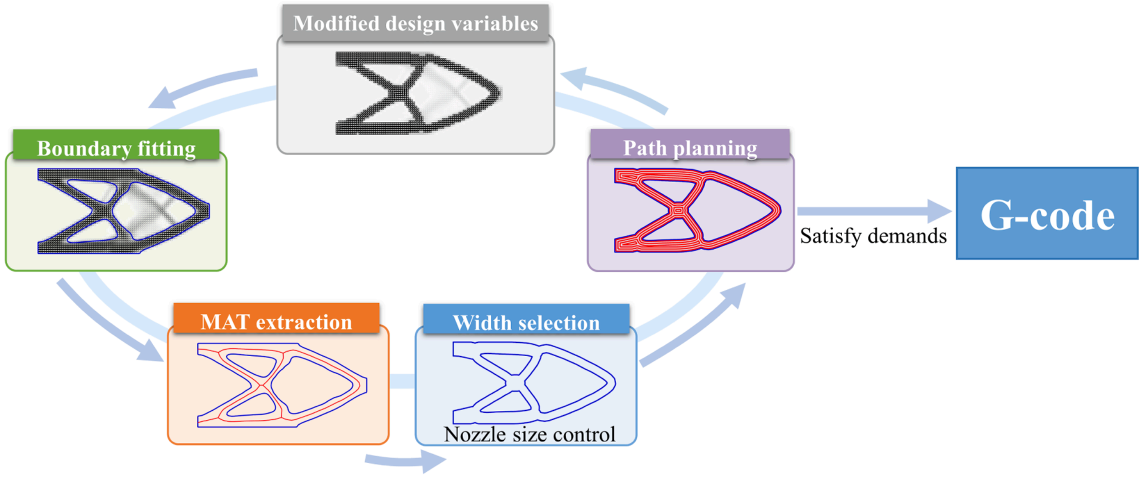

Fig. 5. The incorporation of the adaptive nozzle size control.

geometry boundary is constructed, as presented in Fig. 6(a). The medial axis of the structural form is obtained through the locus of the center of the maximal disk within the polygon interior and the obtained result corresponds to multiple short lines. Then these short lines are connected to some long lines with intersections. In Fig. 6(a), the black lines denote the domain boundary, blue lines denote the domain triangles, and red lines denote the medial axis. Observe that there are some minor branches at the end of the structure, which are incompatible with the structural form. These minor branches must be removed to avoid misleading structural optimization. Therefore, short lines with smaller lengths and no connection at one end are removed to obtain the main branches, as shown in Fig. 6(b). If all segmented medial axes are connected at both ends, the central axis can be considered as the final result. If there remains an unconnected section, it is necessary to extend this type of line to ensure that the medial axis precisely fits the structure form. Because one end of each central axis branch is open, the line segment must be extended until it intersects with the nearest boundary, as shown in Fig. 6(c). The final result of the medial axis extraction is shown in Fig. 6(d).

(3) Adaptive width selection for each segmented central axis.

After obtaining the final medial axis extraction result, the process to obtain the new structural form via offsetting the adaptive width should be performed, as shown in Fig. 7. In Fig. 7(a), the width of each segmented central axis is calculated by drawing an inner tangent circle, with the point on the central axis taken as the center that intersects the geometry boundary. The circle diameter d corresponds to the desired width. Because each branch of the structural form is not of the same width, the line segment is divided into intervals and the width of the segmented central axis is characterized by the diameter corresponding to these segmentation points. Accordingly, 50 intervals are adopted in this study. The geometric features of this part are efficiently obtained by calculating the 50 corresponding width values separately. Because the corresponding widths of the two ends of the central axis are relatively large, which is shown in Fig. 7(b) and taking the average of all values will lead to an inaccurate width selection. Therefore, the central axis width of this segment is determined by the K-medoids clustering analysis method, which avoids the adverse effects of outlier data on the clustering results. The distribution of silhouette coefficient values is used to

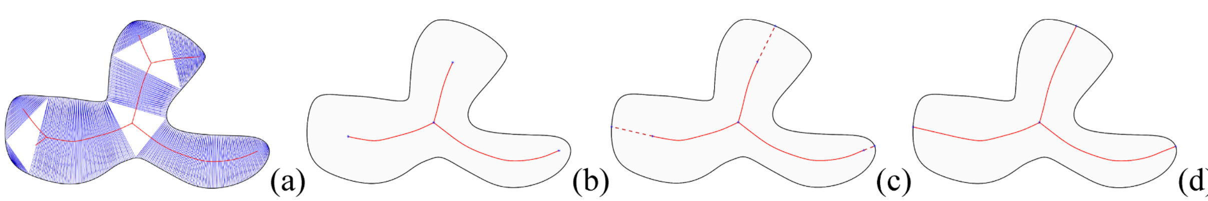

Fig. 6. The process of medial axis extraction: (a) the constrained Delaunay triangulation result, (b) the medial axis without minor branches, (c) the medial axis with extended branches and (d) the final result of the medial axis extraction.

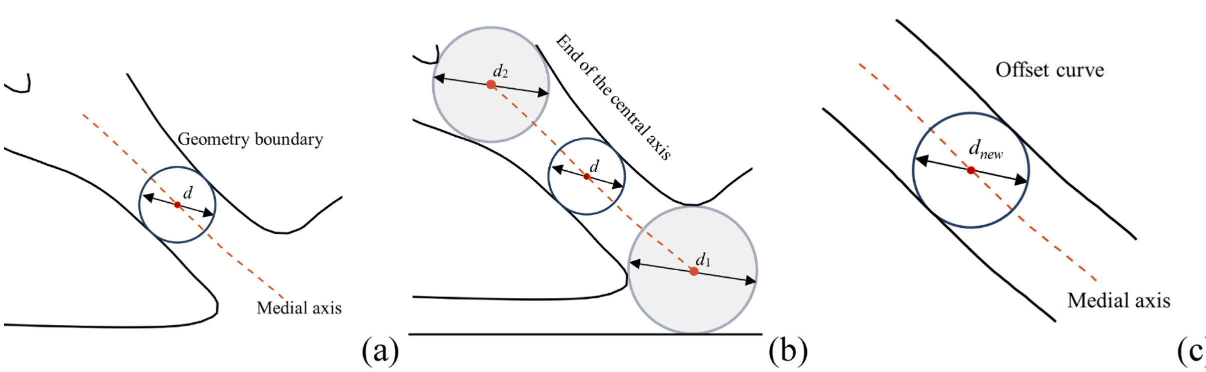

Fig. 7. The calculation of the final width for a certain central axis: (a) the width calculation of the central axis, (b) inner tangent circles at the end of the central axis and (c) the final structural form of the certain central axis.

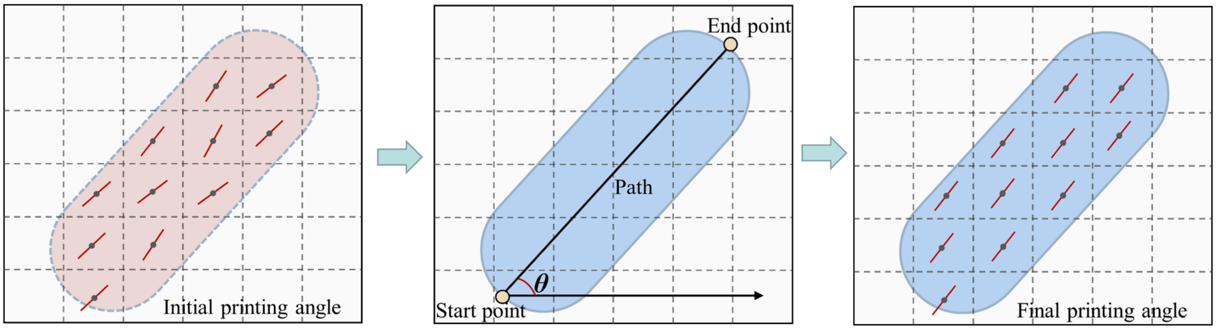

Fig. 8. The process of assigning the printing angle.

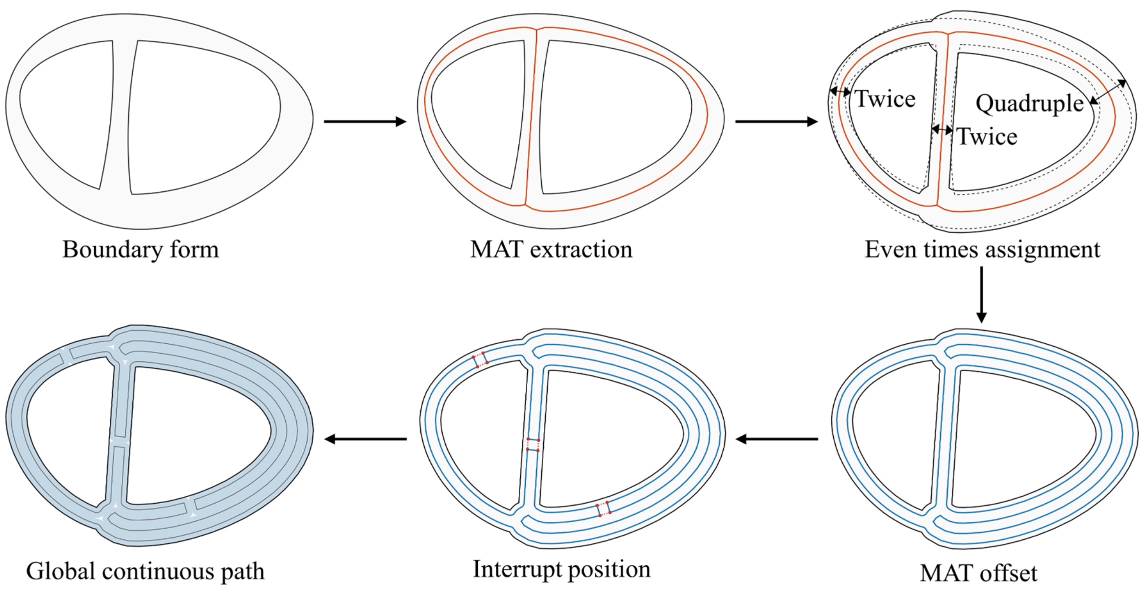

Fig. 9. The flowchart of path-continuity control.

evaluate the quality of the clusters. If most values in both clusters have a large silhouette value, namely, greater than 0.8, this indicates that those values are well separated from the neighboring clusters. The final width d_{new} of the segmented central axis can be selected, and the offset of the segmented medial axis is performed according to the final width setting values to obtain the new structural form, as shown in Fig. 7(c). The nozzle size control for each branch can be expressed as follows:

$$\begin{aligned} & d_{new,i} = d_{p,i}, i = 1, 2, ..., n \\ & \left| d_{p,i} - d_{k,i} \right| = \min_{j=1,2,...,m} \left| d_j - d_{k,i} \right| \end{aligned} \tag{9}$$

where $d_{new,i}$ is the width of i^{th} branch and n is the total number of branches; d_j is the j^{th} candidate of the discrete width values of different multiples out of m candidates; $d_{k,i}$ is a value that represents the i^{th} branch's width, which is a clustered value of the current branch's width. The MATLAB function for K-medoids clustering is adopted to obtain the $d_{k,i}$ value. In this paper, the values are divided into two clusters, and the cluster with more numerical distribution is the final width result.

(4) Offset path planning of the obtained structural form.

After the adaptive width selection of all segmented central axis, a new structural form that meets the nozzle size is obtained. Because the design variables for the printing angle are based on the elements and are not combined with the real printing path, the optimized results can only roughly represent the printing direction. To effectively combine the path planning results, offset path planning is performed on the obtained structural form to correct the printing angles.

(5) Modification of design variables after incorporating the nozzle size control.

Finally, the corresponding results are incorporated into the iterative process, and the design variables are modified. Because the design variable of printing angle is based on elements, the angles characterizing the printed strip from the current printing point to the next point are different. However, the angles in the actual printing are fixed. To better fit the actual printing process, the printing angle in the printed strip is varied with respect to the slope corresponding to the tool-path, as illustrated in Fig. 8. To avoid the oscillation of the optimization iteration caused by the 0–1 change in the element density, the initial element density is averaged with respect to the element density obtained by the medial axis offset and serves as the initial value of the next optimization iteration.

Through the above steps, the nozzle size control can be successfully introduced into the optimization iteration process. The final optimization results can be obtained after repeated iterations.

2.3. Path-continuity control of 3DCP

To simplify the structural geometrical features, the central axis divides the complex structure into multiple small branches. If the corresponding width of each sub-branch is an even multiple of the nozzle diameter, multiple closed-loop subregions can be generated through the offset path and the paths of subregions are connected by one stroke, corresponding to the “go and back” strategy presented by Jin et al. [40]. The generation of a global continuous path must interrupt the offset path first and then connect based on the weighted undirected graph

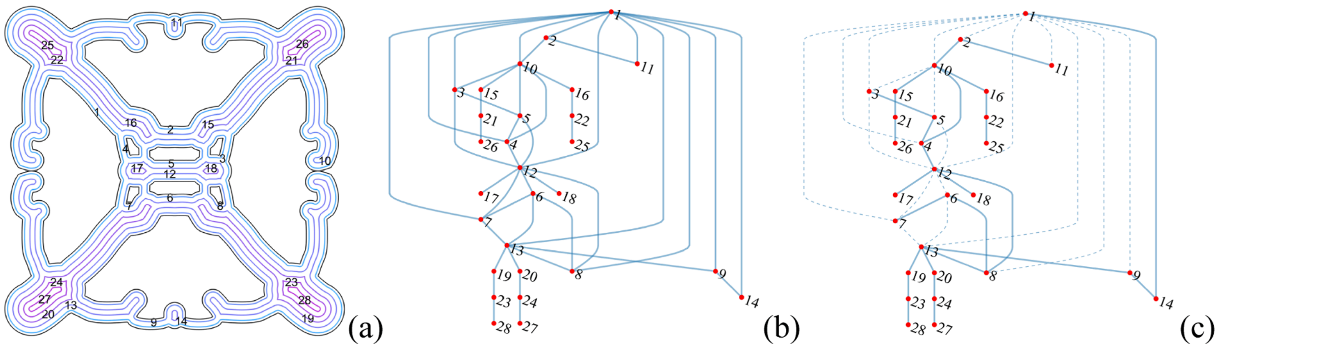

Fig. 10. Construction of the path connection order: (a) the distribution and number of sub-paths, (b) the adjacent graph of sub-paths and (c) the final connection diagram of sub-paths.

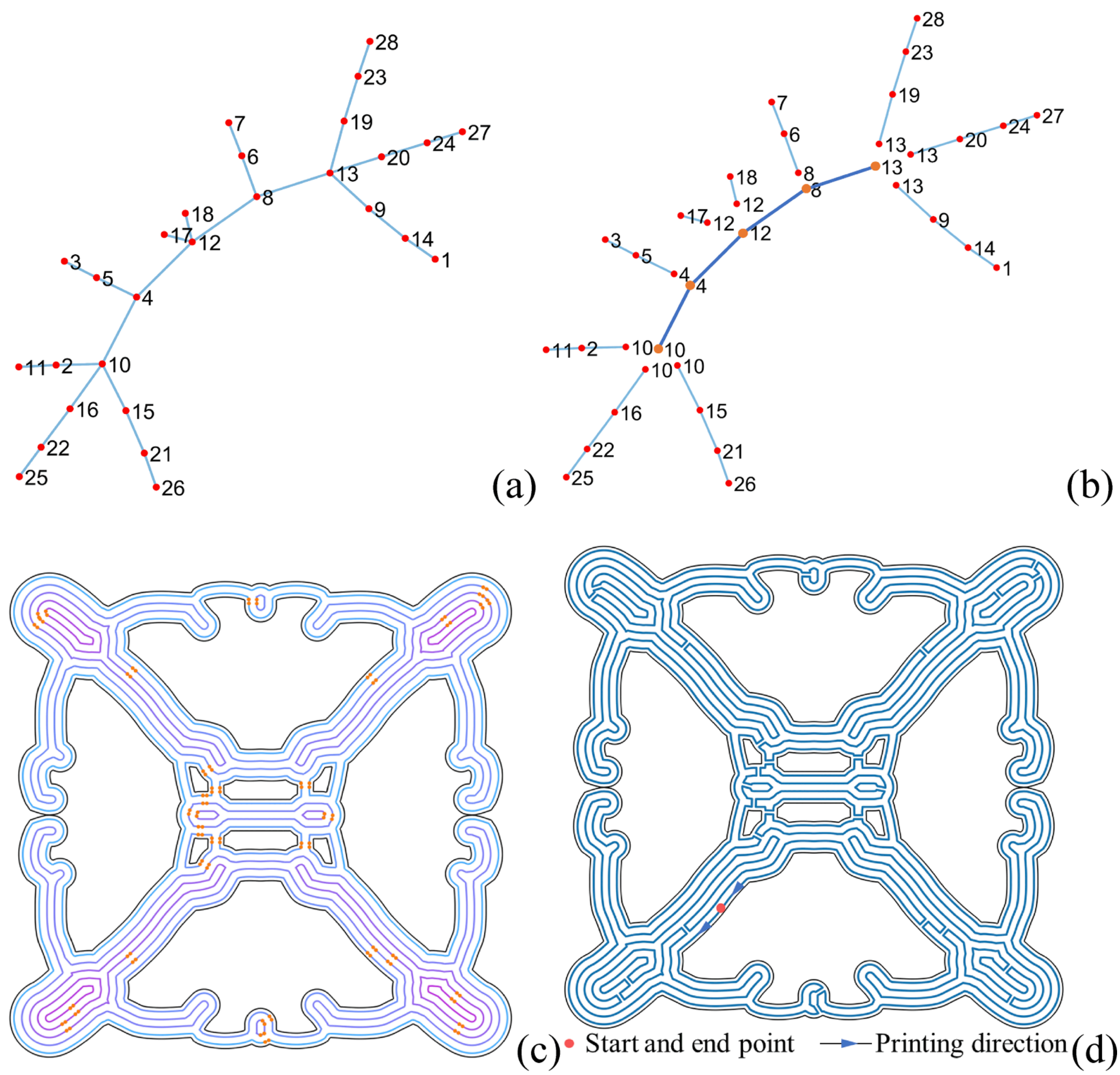

Fig. 11. The flow chart of global path connection: (a) path connection order, (b) path classification, (c) path connection points and (d) one-stroke path.

combined with minimum spanning tree and closest point principle. The corresponding flowchart is shown in Fig. 9.

Breaking and reconnecting at any position is possible for a small number of segmented closed paths. However, in the case of multiple closed and connection paths, there are various schemes for interrupting and reconnecting owing to the complexity of the connection between segmented paths. To choose the interrupted position of closed paths more reasonably and ensure the continuity of the path planning in the designed structural components, the one-stroke printing connection method is proposed. A weighted undirected graph combined with the minimum spanning tree of the graph is used. The weight is related to the length of the two adjacent paths. The specific selection process is illustrated in Fig. 10. First, multiple closed sub-paths are generated through the offset path and numbered for path planning, as shown in Fig. 10(a).

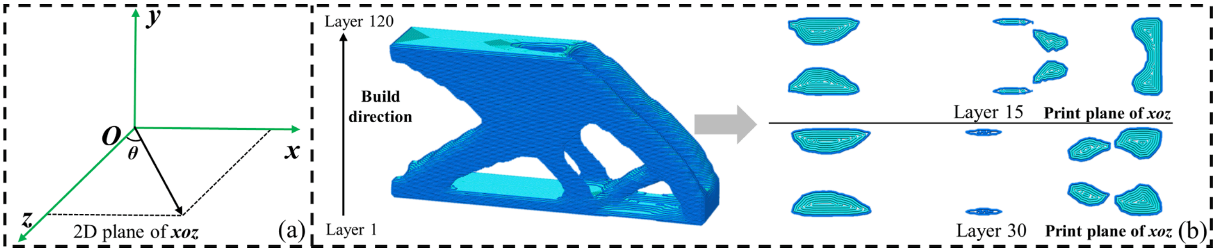

Fig. 12. Schematic of: (a) printing angle control and (b) closed region control in the print plane for 3D structures.

Table 1
Fiber reinforced concrete material properties.

E_1	E_2	G_{12}	ν_{12}	X_t
43.2 GPa	30.7 GPa	14.6 GPa	0.2	8 MPa
X_c	Y_t	Y_c	S_{12}	S_{23}
144.2 MPa	4 MPa	90.4 MPa	12 MPa	12 MPa

Then, the adjacency relationship of sub-paths and alternative path connection schemes is obtained by drawing the undirected graph, as shown in Fig. 10(b). It can be seen that there are many connection schemes, and it is very important to choose the most effective one. Therefore, the path connection order is determined via the weighted undirected graph combined with the minimum spanning tree of the graph, as shown in Fig. 10(c), where the solid lines represent the connected order.

The flow chart of the path connection is shown in Fig. 11. After obtaining the path connection order (Fig. 11(a)), further classification, including the main and branch paths, is performed according to the degree of the numbered nodes. The main path is obtained through these connections such that the node degree is greater than two. The dark blue lines represent the main path, while the light blue lines represent the branch path, as shown in Fig. 11(b). Then, the interrupted points based on the main and branch paths are obtained in order. The interrupted points between every two paths adopt the closest-point principle and then are offset to both sides to obtain two lines. The intersections of the four lines denote the interrupted points. The orange points in Fig. 11(c) are the interrupted and reconnected positions. Finally, the one-stroke path form is obtained by the interruption and reconnection of the sub-paths, as shown in Fig. 11(d).

2.4. Printing angle and closed-region control of 3DCP

First, the print plane needs to be determined because 3DCP operates in a layer-by-layer manner. The printing angle θ denotes the angle between the printing path and positive direction of the x-axis, which changes only within the print plane, as shown in Fig. 12(a). Then, owing to the degrees of freedom in the 3D structure design, it is easy to obtain multiple disconnected closed areas in the printing layer, denoted as the island problem, which should be addressed. There is no island phenomenon in the optimization problem of a 2D structure to conform to the force transmission. However, when slicing 3D optimized components to realize path planning, the island problem is prone to occur in the print plane, which is presented in Fig. 12(b). It can be seen that there are some independent regions of the 15th and 30th layers leading to many breakpoints in the printing process. Therefore, connectivity

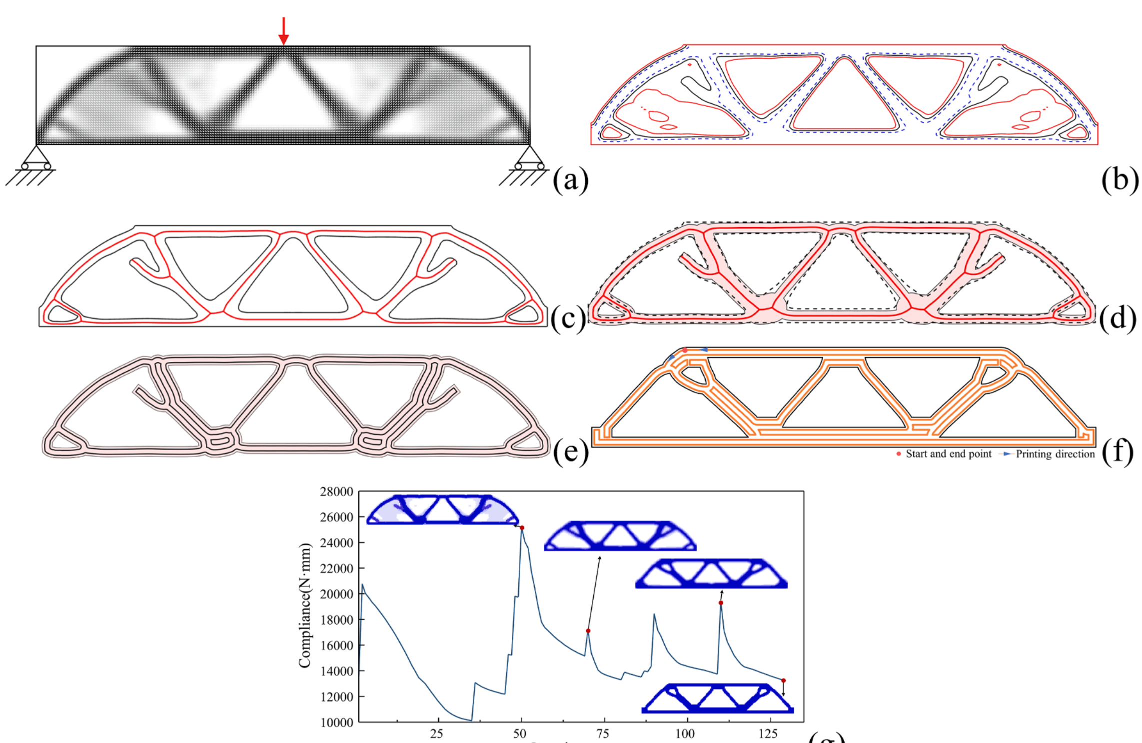

Fig. 13. The process of imposing nozzle size: (a) initial form of design variables, (b) contour plotting results for different density values, (c) medial axis of structural form, (d) new structural form, (e) path planning result, (f) final form and (g) the convergence history.

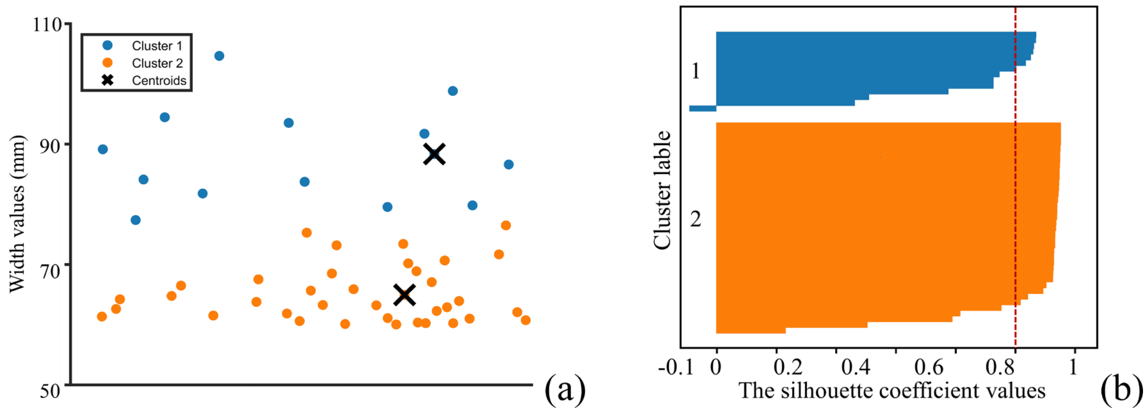

Fig. 14. Accuracy evaluation of clustering results: (a) clustering results of width values and (b) the silhouette coefficient values.

should be ensured in the print plane to ensure one-stroke printing. The closed region control states that the number of closed regions of each printing layer is one.

The printing angle control can be achieved by changing the angle in a specific print plane. The addition of this control affects the solution of the elastic matrix obtained by calculating the rotation matrix $\boldsymbol{T}$ and changes the design variables during the optimization iteration by affecting the sensitivity values. The addition of closed region control is presented in detail in the research published by Bi et al. [25]. Some closed regions are connected to generate an enclosed 2D geometry in each layer. This study mainly realizes the application of connectivity control through MATLAB functions, such as *bwconncomp*, *labelmatrix*, *label2rgb*, and *bwdist*, and the shortest path finding algorithm used for achieving a one-stroke path planning on a certain printing layer.

3. Validation of the proposed integration method

Numerical examples are provided in this section to confirm the applicability of the proposed integrated design method regarding the topology and printing path. Each section illustrates the manner in which different controls are reflected in the optimized design. For all examples, the material properties of fiber-reinforced concrete are listed in Table 1. To avoid the change process of element density from the intermediate density to 1 in the regions where materials need to be laid, the initial design variables of the element density and printing angle were set to 1 and 0, respectively. Moreover, move limits were adopted to restrict the maximum amplitude of change for a design variable to avoid oscillation of objective values during the iterative process. The move limit parameters were set to 0.1 and $\pi/9$, respectively.

3.1. Validation of nozzle size control

The nozzle size control should not be introduced prematurely in the optimization process for two reasons. On the one hand, the boundary form cannot effectively represent the structural force if there are too many intermediate-density elements. On the other hand, the modified design variables based on path planning will mislead the subsequent optimization iteration. Note that after introducing the size control, the printing angle filtering during the optimization iteration should eliminate the part with a large difference from its value; otherwise, it will affect the continuity of the angle, and the optimization result cannot converge. For the extraction and offsetting of the central axis near the design domain boundary, the boundary corresponding to the central axis should be selected for the offsetting to ensure that the resulting result is contained within the design domain.

As shown in Fig. 13, a beam case under three-point bending is used to describe the process of imposing a nozzle size control for topology optimization. At the 50$^{\text{th}}$ iteration, the nozzle size control is introduced. The initial element printing angle and density distribution are shown in Fig. 13(a). Observe that the material distribution is generally determined, and the printing angle lies mostly along the force transfer path, meeting the criteria for introducing the nozzle size control. Then, a

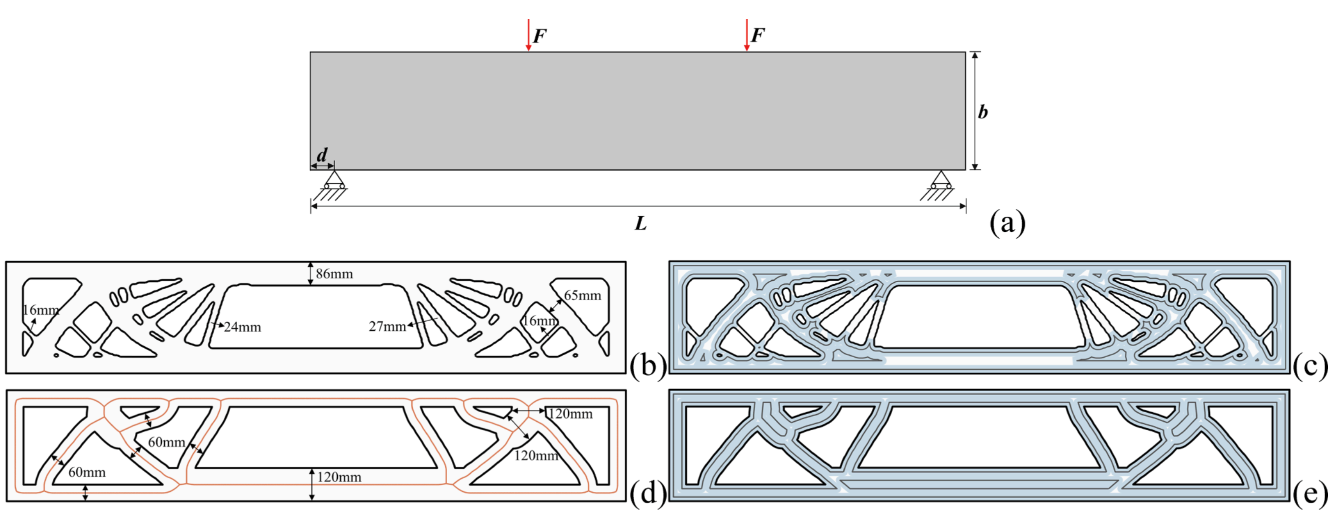

Fig. 15. Topological design of a four-point bending beam: (a) boundary/load conditions, (b) optimized structural configuration and (c) planned path without nozzle size control; (d) optimized structural configuration and (e) planned path with nozzle size control.

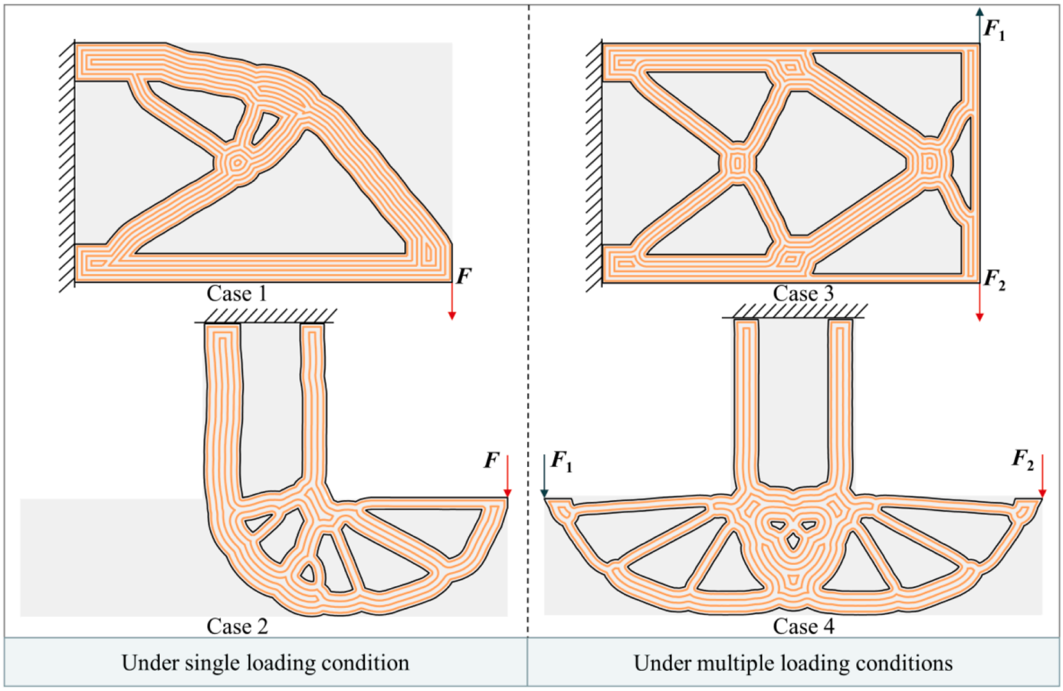

Fig. 16. Different cases for the nozzle size validation.

contour plotting algorithm is executed, as shown in Fig. 13(b), where different types of lines denote the contour plotting results for different density values. The red solid, black solid, and blue dotted lines denote the contour for a density value of 0.7, 0.5, and 0.3, respectively. In this case, a value of 0.5 is applied to determine the contour boundary because it is closer to the material distribution pattern. Note that it is also feasible to set the threshold at 0.3 or 0.7. The obtained structural forms exhibit the same force transmission path. There is only a small difference in the width of some local positions, and the optimization iteration time is longer. Then, the medial axis of the structural form is extracted (Fig. 13(c)). The width of each segmented central axis is obtained using the K-means clustering algorithm; the obtained structural form is shown in Fig. 13(d). Then, the contour-parallel offset path form is generated to obtain the new printing angle, which is presented in Fig. 13(e). When the number of optimization iterations is 130, the final integrated design obtained after applying the nozzle size control is shown in Fig. 13(f). The convergence history is shown in Fig. 13(g). Notice that the objective function will increase significantly before and after the nozzle size control is applied, which is due to the large change in element density. Because subsequent optimization will be conducted, it will not significantly affect the final result. Meanwhile, the introduction of the nozzle size control accelerates the change in element density and the final result can be obtained with fewer optimization iteration steps.

To evaluate the accuracy of the clustering results, a branch is selected for statistics and data analysis, as shown in Fig. 14. The geometric features of this branch obtained by calculating the 50 corresponding width values separately. The width values are divided into two clusters, and the centroids of each cluster are located at 88.34 mm and 64.95 mm, respectively, as shown in Fig. 14(a). To evaluate the quality of the clusters, the distribution of silhouette coefficient values was used, as shown in Fig. 14(b). Notice that most silhouette coefficient values are greater than 0.8, ensuring the accuracy of clustering and indicating that those values are well-separated from neighboring clusters. The clustering results are reliable and can be used for the nozzle size control to provide relevant directions for the change in design variables in the optimization iteration.

A four-point bending beam example is adopted to validate the effect of the nozzle size control on the topology optimization design. The dimensions and boundary/load conditions are shown in Fig. 15(a), where L = 2200 mm, b = 400 mm, d = 80 mm, and F = 30 kN. The design domain is discretized using four-node square elements with a side length of 5 mm. The nozzle size is set to 30 mm. A non-design domain with a width of 2 × nozzle width is set to facilitate the actual application. The volume fraction is set to 40 % of the design domain.

For the optimized results without the nozzle size control, the branches have different widths ranging from 16 to 86 mm, and some widths are less than the manufacturing precision, that is, the size of the nozzle (30 mm), as shown in Fig. 15(b). Fig. 15(c) shows the path of the optimized design without the nozzle size control. Here, the filling rate is 53.84 %, indicating poor printing quality.

On the contrary, for the optimized results with nozzle size control, each branch width satisfies an even multiple of the nozzle diameter, and all areas can meet the manufacturing requirement, as shown in Fig. 15(d). Thus, the design result is relatively simple and suitable for 3DCP. Fig. 15(e) shows the path of the optimized design with the nozzle size control. The filling rate is 99.37 %, which is 85 % higher than that without considering the nozzle size control. Comparing the results with and without size control, notice that the main regions of material distribution are similar, but tiny branches are removed through the nozzle size control. Path planning can ensure a high filling rate and achieve consistency in the design and manufacturing results. Compliance values are also compared. The value without considering the manufacturing constraints is 22,532 N·mm and the value considering the manufacturing constraint is 26,509 N·mm, implying an increase of approximately 17.65 %.

Four cases are selected to verify the applicability of the proposed method, as shown in Fig. 16. The ratio of the real printed area to the design model area is the filling rate and the filling rates of the four cases are 99.73 %, 99.20 %, 99.44 %, and 99.34 %, respectively. Observe that this method can realize integer multiple control of optimization design results under single and multiple loading conditions, realizing a high filling rate of the printed components.

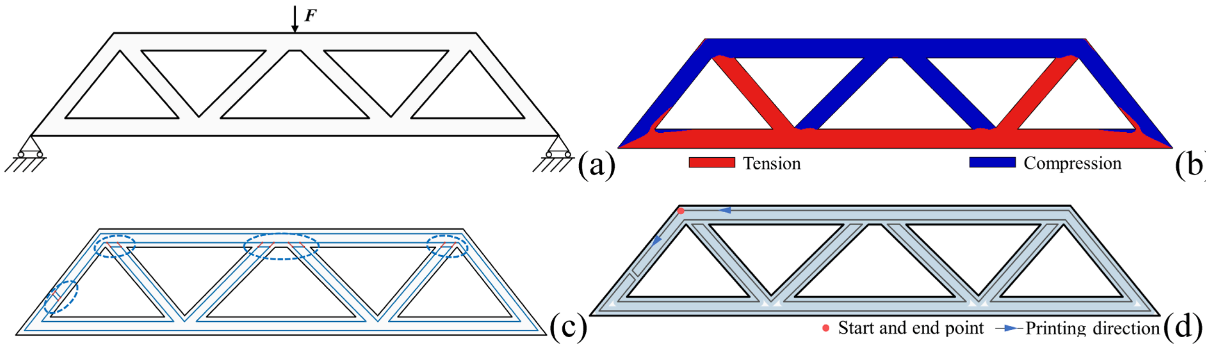

Fig. 17. The flow chart of path connection according to the stress distribution: (a) component form, (b) the distribution of stresses, (c) the distribution of breakpoint positions and (d) the final one-stroke path.

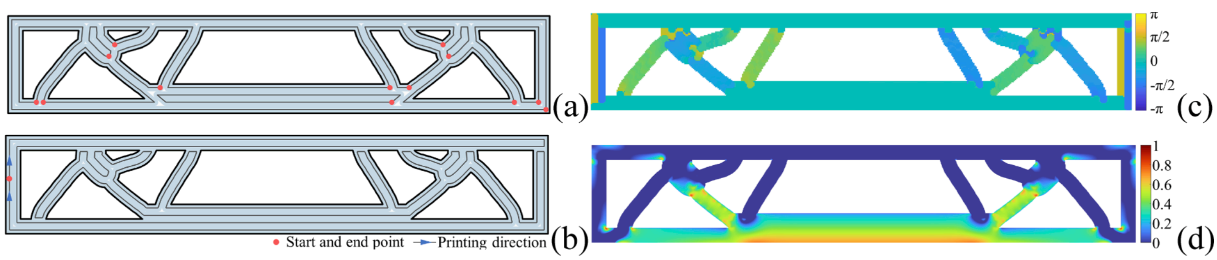

Fig. 18. The paths without and with the path-continuity control: (a) offset path without the path-continuity control and (b) one-stroke path with the path-continuity control. The distributions of (c) printing angles and (d) Tsai-Wu values for the printed beam.

3.2. Validation of path-continuity control

In Section 3.1, the design result obtained considering the nozzle size control is presented. However, the offset path contains breakpoints that require multiple startups and shutdowns, which is not suitable for 3DCP structures reinforced by continuous micro-cables [41]. Meanwhile, the breakpoints are weak areas prone to structural damage.

For optimized components with obvious tension and compression areas, the breakpoint positions should be distributed at the ends of each member as much as possible to ensure that the breakpoints do not appear in the tension area. The criterion for assessing the tension areas is that the sum of the first and third principal stresses is greater than 0. In contrast, the remaining part corresponds to the compression area. Fig. 17(a) shows the optimized three-point bending component, and Fig. 17(b) shows the distribution of the tension and compression areas. The red part represents the tension area, while the blue part represents the compression area. The distribution of breakpoint positions is shown in Fig. 17(c), and the final one-stroke path that ensures the continuity of the force transmission path within the structure is shown in Fig. 17(d).

The paths with and without the path-continuity control are shown in Fig. 18. The offset path without the path-continuity control is shown in Fig. 18(a). The size of the design domains is the same as Fig. 15. The red dots indicate the positions of startups and shutdowns for each sub-path. The number of sub-paths is 13, which hinders to the performance of the structural component. Breakpoints can be avoided by incorporating the path-continuity control. Because the optimized four-point bending beam has clear tension and compression areas, the reconnection positions are selected at the end of each member and do not appear in the tension area. The one-stroke path with the path-continuity control is presented in Fig. 18(b) and the start point of the path can be selected randomly. The filling rate is 99.79 %, approximately 100 %, achieving a high filling of printed components. The printing quality of the component is significantly improved owing to the one-stroke path, and the number of printing defects is reduced. Meanwhile, the path planning results are consistent with the optimal force transfer path obtained by topology optimization, which is beneficial for obtaining higher structural

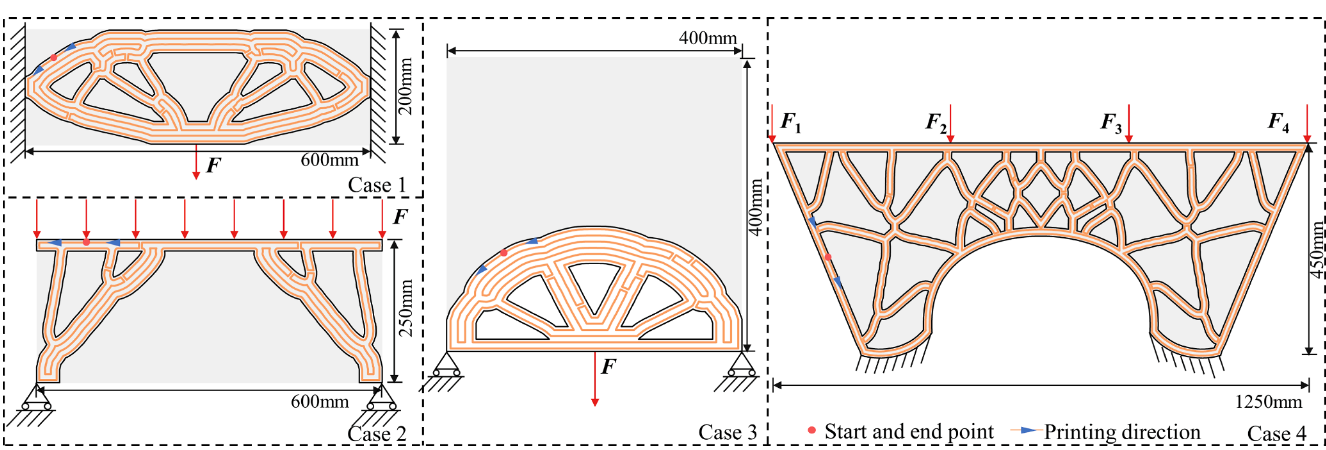

Fig. 19. Different cases for the path-continuity validation.

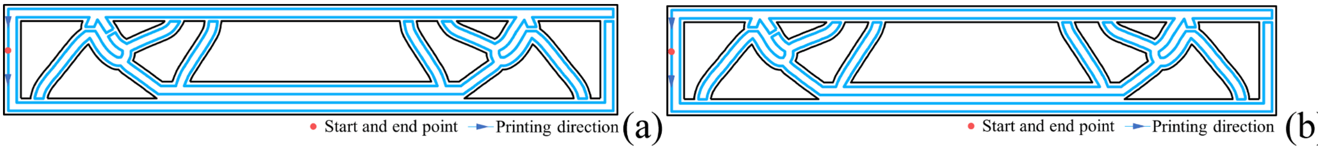

Fig. 20. The optimized result at different iterations for introducing the nozzle size and path-continuity controls for the first time: (a) 0 and (b) 20.

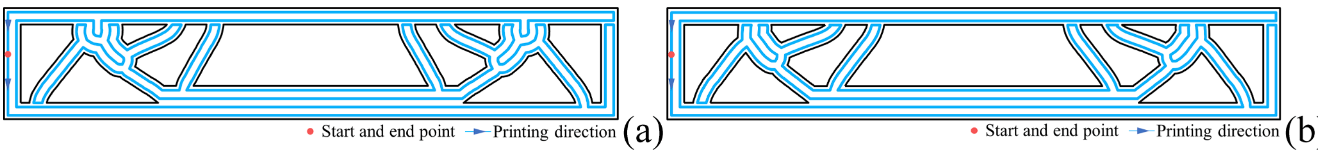

Fig. 21. The optimized result with different intervals for introducing the nozzle size and path-continuity controls: (a) 10 and (b) 30.

performance.

To evaluate the strength of the printed components, the distributions of the printing angle obtained by the one-stroke path are presented in Fig. 18(c). The corresponding Tsai-Wu values based on the printing orientations are shown in Fig. 18(d). According to these results, the Tsai-Wu values are less than 1. This indicates that there is a problem with stress concentration at the printing corner, mainly owing to the poor continuity of printing angles in these regions, which can easily cause structural damage. However, in the actual printing process, the areas located at the corner can be strengthened through the accumulation of materials and may be protected against potential damage during the practical application process.

As shown in Fig. 19, four cases in which the design domain is discretized by four square node elements with a side length of 5 mm are selected to validate the path-continuity and the nozzle size is set to 10 mm, which can realize the printing of optimized components with high filling rates and a one-stroke path to improve the performance of printed components.

To further verify the robustness and potential drawbacks of the proposed method, a discussion of the parameter sensitivity on the number of iterations for the first time and different intervals for introducing modifications of the nozzle size and path-continuity controls is implemented. Firstly, the optimization results for introducing design variable modifications at different iterations, including 0 and 20, are carried out, which is shown in Fig. 20. In the first case, the optimization is terminated at the 160^{th} iteration, and the modifications are made 9 times in total. The final objective function value is 25,702 N·mm. In the second case, the optimization is terminated at the 140^{th} iteration, and the modifications are made 7 times in total. The final objective function value is 25,612 N·mm. Through the comparison, it can be seen that the premature introduction of modifications will make the calculation time longer, but the final optimized results are basically the same, and the objective values are similar. Therefore, introducing design variable modifications for the first time at different iterations can obtain satisfactory optimization results.

Then the optimization results with different intervals for introducing the nozzle size and path-continuity controls are carried out, including 10 and 30. The first case is terminated at the 80^{th} iteration and the final objective function value is 25,903 N·mm. In the second case, the optimization is terminated at the 140^{th} iteration and the final objective function value is 25,931 N·mm. Four modifications of the design variables are made in both cases. Fig. 21 shows the optimized results for both cases. It can be seen that the final optimization results and the structural force transmission paths are basically the same, and there are only differences in local positions. It is worth noting that the final result cannot be obtained by modifying the design variables at every iteration. This is because when the element density is changed once, the corresponding structural central axis is basically unchanged and it is impossible to modify the design variables. At the same time, it is not recommended to have too many iterations occur between the interruption. This is because the structure is too clear, and it is easy to cause too much material to be reserved after introducing design variable modifications, which is not conducive to the satisfaction of volume constraint.

3.3. Validation of manufacturing constraints for 3D structures

This section describes the effect of manufacturing constraints for 3D structures on topology optimization design. First, the effect of imposing the closed region control is shown in Fig. 22. The middle layer result of the topology optimization plate considering the overhang control is presented in Fig. 22(a). The different colors in Fig. 22(a) represent different blocks, and serious island problems are illustrated. If this structure is printed, there will be a large number of breakpoints, which

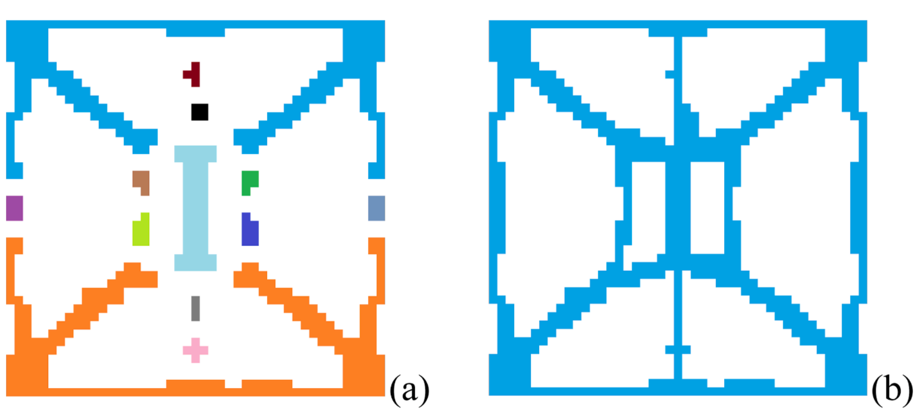

Fig. 22. Effect of imposing closed region control: (a) result with island problems and (b) result with closed region control.

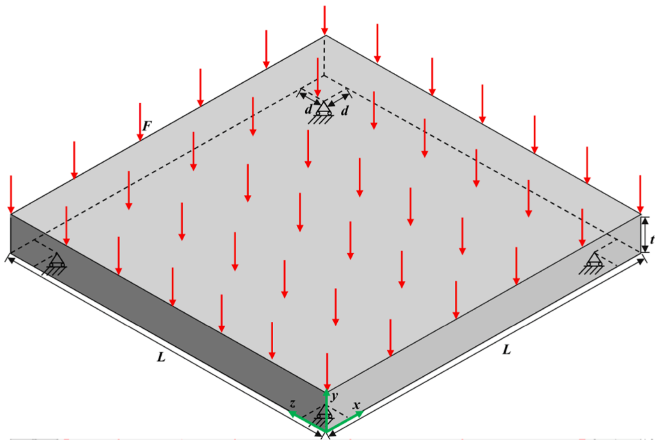

Fig. 23. Dimensions and boundary/load conditions of a 3D plate structure.

shows that the overhang and closed region controls are the basis for realizing the one-stroke forming of the printing layer. First, we determine the two blocks with the shortest connected distance, then connect them to form a new block, and repeat the process until there is only one closed region. The final result obtained with the closed region control is shown in Fig. 22(b). By comparing the two graphs, we determined that the disappearance of the island problem after adding the closed region control could guarantee a one-stroke path within the printing layer.

Then, the optimized example of a 3D plate structure with a uniform load is used to prove the necessity of introducing manufacturing constraints (e.g., nozzle size, path continuity, close-region, and overhang controls) for the 3D structure. The dimensions and boundary/load conditions are shown in Fig. 23, where $L = 900$ mm, $t = 100$ mm, $d = 60$ mm, and $F = 15$ kN/mm^2. The nozzle size was 30 mm, and the printing layer thickness was 20 mm. The design domain was discretized by eight-node hexahedral elements with an element size of 10 mm $\times$ 20 mm $\times$ 10 mm. The volume fraction was set to 50 % of the design domain.

The traditional design and manufacturing results for the 3D optimized plate are shown in Fig. 24. The topology optimization design and path planning for each layer of the 3D plate structure are presented in Fig. 24(a) and (b), respectively. Observe from Fig. 24(b) that there is an island problem with a disconnected region in a layer. The unfilled and overfilled areas cause structural defects because each branch varies in width. Because of the design pattern of layer 5, there are many supporting areas, and the supporting materials cannot be effectively removed. Notice that the print quality of the optimized components cannot be guaranteed. Therefore, a design without manufacturing constraints is not suitable for 3D printing.

Considering the structural geometry and force characteristics, the *x*-*z* coordinate plane is taken as the print plane of layer extrusion and negative *y*-direction as the build direction. Because this is a multi-constraint control problem, there is a sequence problem. The anisotropic behavior and overhang control are applied at each iteration. After a certain step of the optimization iteration, the closed region control is first applied, then the nozzle size control is applied and design result with path planning is obtained by multiple optimization iterations. The final results of the 3D optimized plate obtained by the proposed method are shown in Fig. 25. The convergence history is shown in Fig. 25(a), which shows that the application of the overhang control significantly changed the structure form, which determined the force transmission path earlier, and other manufacturing constraints only altered the optimization results. The 3D design pattern is shown in Fig. 25(b). Unlike conventional optimized design, there is no island phenomenon to ensure the continuity of printing. The one-stroke path presentation forms of each layer are shown in Fig. 25(c). Observe that the optimization results of each layer are integer multiples of the nozzle diameter and there is no supporting material, which effectively satisfies the design requirements. Fig. 25(d) shows the corresponding distribution of the Tsai-Wu values for each printing layer. It is shown that structural damage does not occur, and the bottom of the plate is more prone to damage, which is consistent with the actual situation.

To further verify the advantages of considering manufacturing constraints in the topology optimization of 3D structures, Table 2 lists the filling rate and breakpoint number values of the different printing layers of Figs. 24 and 25. Comparing the filling rates, the result obtained with constraints are greater than those without constraints. Breakpoints disappear owing to the addition of the path-continuity control, which achieves the one-stroke path. The problems of traditional topology optimization design and manufacturing results are successfully resolved, such as poor fill rate, breakpoints, and supporting materials. The proposed method can successfully integrate the design and construction, and directly obtain an optimized pattern with a one-stroke path.

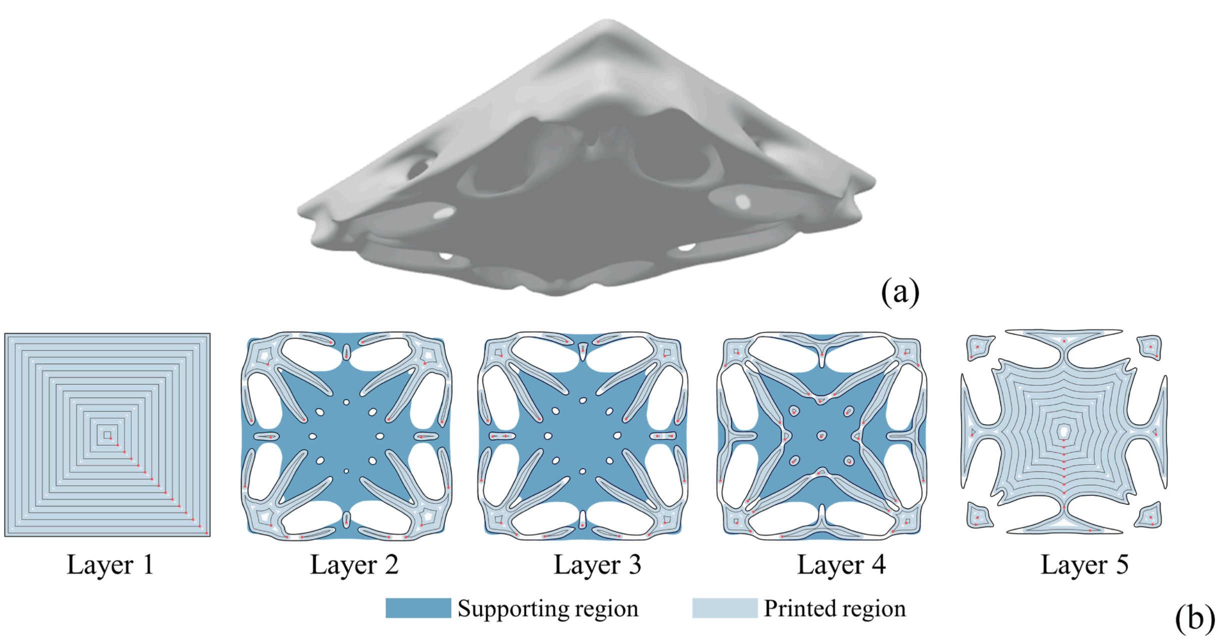

Fig. 24. The traditional design and manufacturing process for 3D optimized plate: (a) topology optimization design and (b) path planning of each layer.

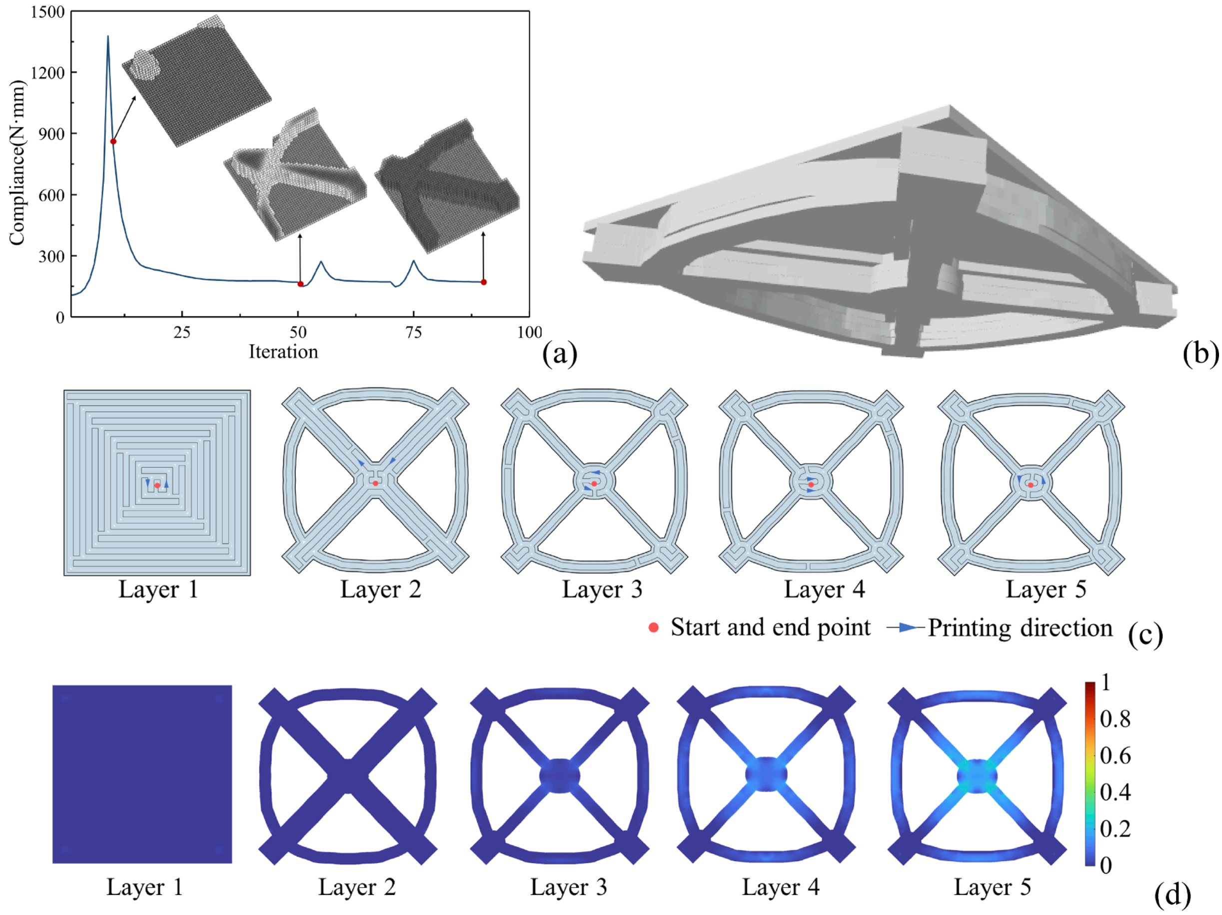

Fig. 25. The results of proposed method for 3D optimized plate: (a) the convergence history, (b) integrated design result, (c) path planning and (d) Tsai-Wu value distribution of each layer.

Table 2
The filling rate and breakpoints number of different printing layers.

Different printing layers	Layer 1	Layer 2	Layer 3	Layer 4	Layer 5
Fill rate value without constraints	99.64%	92.32%	87.07%	90.15%	95.26%
Fill rate value with constraints	99.68%	99.49%	99.49%	99.50%	99.54%
Breakpoints number without constraints	15	20	22	29	21
Breakpoints number with constraints	0	0	0	0	0

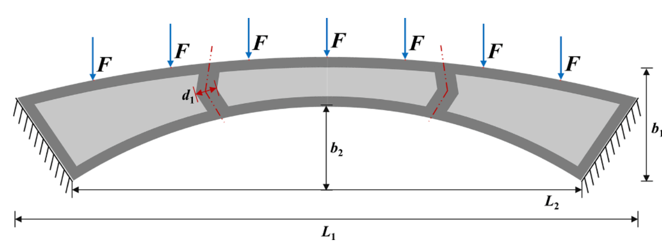

Fig. 26. Dimensions and boundary/load conditions of an arch assembled in sections.

4. Applicability of the integration design method

To verify the applicability of the proposed design method, the design and manufacturing of an assembled arch in sections are investigated. Considering the assembly problem when printing large components, the optimal design is obtained when the assembly scheme is determined. The experiment proves that V-type printed specimens are recommended to be used as the preferred interface connection form at the joints of concrete segmental arch members [42].

The dimensions and boundary/load conditions are presented in Fig. 26, where $L_1 = 5000$ mm, $L_2 = 4100$ mm, $b_1 = 1000$ mm, $b_2 = 600$ mm, $d_1 = 80$ mm, and $F = 10$ kN. Seven concentrated loads are simultaneously applied to the arch case under a single loading condition. Considering that a small element size will increase the calculation time and a nozzle size with a smaller diameter will reduce the printing efficiency, the design domain is discretized by four-node square elements with a side length of 10 mm and nozzle size of 40 mm. Considering the practical application problems, a width of 2 × nozzle width is set as the non-design domain. The volume fraction is 30 % of the remaining domain. The design domain is discretized using four-node square elements.

Fig. 27 shows the optimized results of the single loading condition. The interface connection form was regarded as the non-design domain over the entire optimization process, and path planning was conducted based on different segments in the printing platform. The filling rate of the optimized pattern was 99.56 %, which ensured a high filling rate while realizing a one-stroke path. The distributions of Tsai-Wu values are presented in Fig. 28. All Tsai-Wu values are less than 1, which indicates that the optimized structure has not been damaged under the loading condition. The maximum Tsai-Wu value is 0.78, which is located in the middle of the arch, indicating that the damage will occur first in this region.

To further demonstrate the manufacturability of the optimization

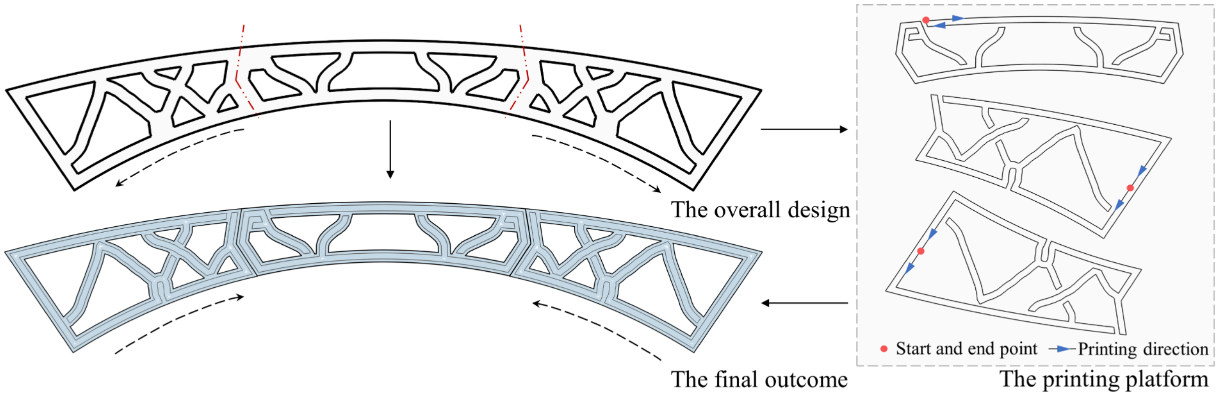

Fig. 27. The optimized results of an arch assembled in sections.

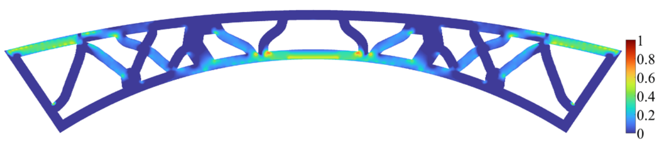

Fig. 28. The distributions of Tsai-Wu values for the arch assembled in sections.

results obtained by the proposed method, the construction of an arch assembled in sections owing to the size limitation of the printing platform is conducted, as shown in Fig. 29. The optimized arch is printed using a 3D concrete printer, as shown in Fig. 29(a). The printing speed is 50 mm/s, printing layer thickness is 10 mm, and nozzle size is 40 mm. The printing results of the three segments are shown in Fig. 29(b). Subsequently, the three segments are assembled to obtain the entire arch, as presented in Fig. 29(c).

Through the construction and assembly of the integrated design, observe that the optimized results obtained by the proposed method have good constructability, which can not only ensure the lightweight design of concrete structures but also avoid the problems of poor quality of printed components due to breakpoints and low filling rates in the manufacturing process. The proposed method can successfully integrate the topology optimization design and construction. Meanwhile, the arch case demonstrates that the segmented position and assembling form can be preset in advance when large-scale components cannot be printed simultaneously. Then, the design and construction are carried out and segmented assembly is realized.

5. Conclusions

This study proposed an integrated design method for the topology and print path of 3D concrete printing to facilitate the application of 3DCP. The optimized components of the 2D and 3D structures were investigated to validate the effectiveness of the proposed integrated approach. The following conclusions can be drawn:

(i) Compared with the conventional topology optimization design without manufacturing constraints, the proposed method, which ensured the manufacturability of topology optimization designs, demonstrated better consistency in design and manufacturing.

(ii) The one-stroke path avoided the existence of interruption points in the printing process and effectively improved the printing quality. A high fill rate of the printed components could be achieved by introducing manufacturing constraints.

(iii) The proposed method obtained design patterns that satisfied the requirements in both 2D and 3D cases, and the construction of the optimized arch further proved the constructability of the design.

In future research, the current method will be extended to structures with multi-objective optimization. Beyond that, next-step research will

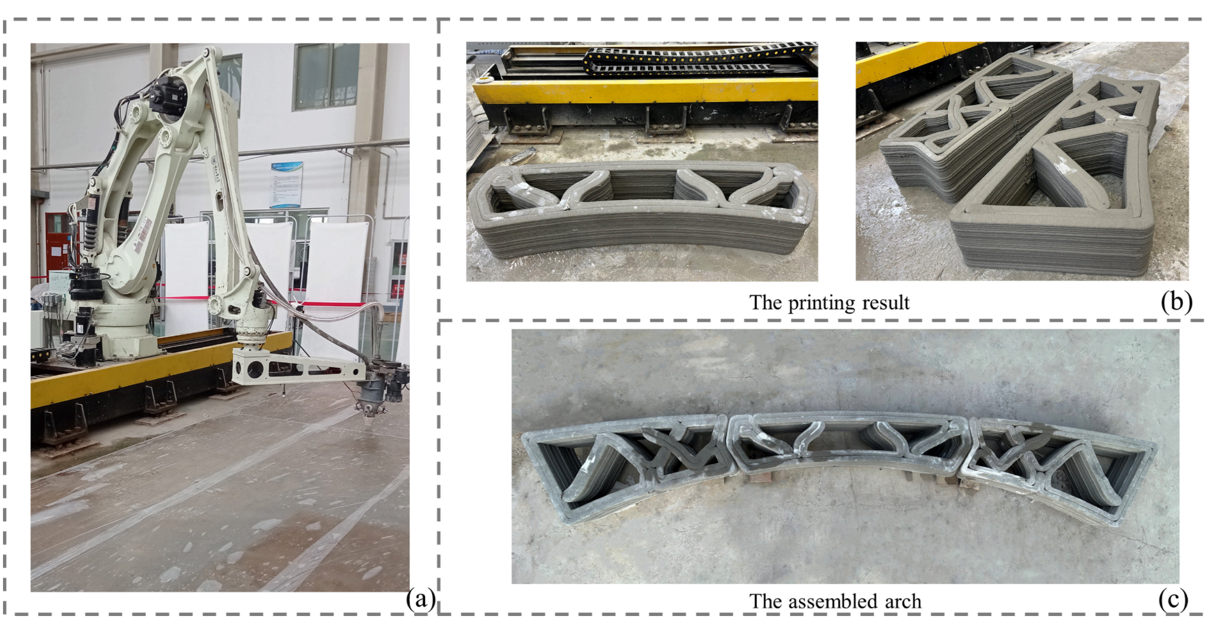

Fig. 29. The construction of an arched case assembled in sections: (a) the 3D concrete printer, (b) printing results of the three segments and (c) the assembled arch.

also focus on experimental validation to verify the proposed method and to prove the addition of manufacturing constraints into the topology optimization framework is promising. Changing the control of even times of nozzle size into integral times with Euler loops should be achieved to decrease the loss of objective values owing to the addition of manufacturing constraints. Meanwhile, it is also necessary to introduce manufacturing constraints for 3DCP in the topology optimization design of reinforced-concrete structures.

CRediT authorship contribution statement

Wenwei Yang: Data curation, Methodology, Investigation, Writing – original draft. **Li Wang:** Conceptualization, Visualization, Writing – review & editing. **Guowei Ma:** Resources, Supervision, Funding acquisition. **Peng Feng:** Supervision.

Declaration of Competing Interest

The authors declare that they have no known competing financial interests or personal relationships that could have appeared to influence the work reported in this paper.

Data availability

Data will be made available on request.

Acknowledgments

The authors would like to acknowledge the financial support from the National Natural Science Foundation of China (No. 52178198, No. U20A20313 and No. 52209158), Natural Science Foundation of Hebei (No. E2021202039 and E2022202041).

References

[1] Ma G, Buswell R, Leal da Silva WR, Wang L, Xu J, Jones SZ. Technology readiness: A global snapshot of 3D concrete printing and the frontiers for development. Cem Concr Res 2022;156. https://doi.org/10.1016/j.cemconres.2022.106774.
[2] Ma G, Li Z, Wang L. Printable properties of cementitious material containing copper tailings for extrusion based 3D printing. Constr Build Mater 2018;162: 613–27. https://doi.org/10.1016/j.conbuildmat.2017.12.051.
[3] Xiao J, Ji G, Zhang Y, Ma G, Mechtcherine V, Pan J, et al. Large-scale 3D printing concrete technology: Current status and future opportunities. Cem Concr Compos 2021;122:104115. https://doi.org/10.1016/j.cemconcomp.2021.104115.
[4] Salet TAM, Ahmed ZY, Bos FP, Laagland HLM. Design of a 3D printed concrete bridge by testing. Virtual Phys Prototyp 2018;13:222–36. https://doi.org/10.1080/17452759.2018.1476064.
[5] Ding T, Xiao J, Zou S, Wang Y. Hardened properties of layered 3D printed concrete with recycled sand. Cem Concr Compos 2020;113:103724. https://doi.org/10.1016/j.cemconcomp.2020.103724.
[6] Gebhard L, Mata-Falcón J, Anton A, Dillenburger B, Kaufmann W. Structural behaviour of 3D printed concrete beams with various reinforcement strategies. Eng Struct 2021;240:112380. https://doi.org/10.1016/j.engstruct.2021.112380.
[7] Bai G, Wang L, Wang F, Ma G. Assessing printing synergism in a dual 3D printing system for ultra-high performance concrete in-process reinforced cementitious composite. Addit Manuf 2023;61:103338. https://doi.org/10.1016/j.addma.2022.103338.
[8] Mesnil R, Poussard V, Sab K, Caron J-F. On the geometrical origin of the anisotropy in extrusion-based 3d printed structures. Eng Struct 2023;275:115082. https://doi.org/10.1016/j.engstruct.2022. 115082.
[9] Feng P, Meng X, Chen J, Ye L. Mechanical properties of structures 3D printed with cementitious powders. Constr Build Mater 2015;93:486–97. https://doi.org/10.1016/j.conbuildmat.2015.05.132.
[10] Stoiber N, Kromoser B. Topology optimization in concrete construction: a systematic review on numerical and experimental investigations. Struct Multidiscip Optim 2021;64:1725–49. https://doi.org/10.1007/s00158-021-03019-6.
[11] Smarslik M, Ahrens MA, Mark P. Toward holistic tension- or compression-biased structural designs using topology optimization. Eng Struct 2019;199:109632. https://doi.org/10.1016/j.engstruct.2019. 109632.
[12] Jewett JL, Carstensen JV. Topology-optimized design, construction and experimental evaluation of concrete beams. Autom Constr 2019;102:59–67. https://doi.org/10.1016/j.autcon.2019.02.001.
[13] Martens P, Mathot M, Bos F, Coenders J. Optimising 3D printed concrete structures using topology optimisation. In: High Tech Concrete: Where Technology and Engineering Meet 2018:301–9. https://doi.org/10.1007/978-3-319-59471-2_37.
[14] Gaudillière N, Duballet R, Bouyssou C, Mallet A, Roux P, Zakeri M, et al. Large-Scale Additive Manufacturing of Ultra-High-Performance Concrete of Integrated Formwork for Truss-Shaped Pillars. In: Robotic Fabrication in Architecture, Art and Design 2018. 2019.:459–72. https://doi.org/10.1007/978-3-319-92294-2_35.
[15] Ooms T, Vantyghem G, Tao Y, Bekaert M, De Schutter G, Van Tittelboom K, et al. The Production of a Topology-Optimized 3D-Printed Concrete Bridge. In: In: Third RILEM International Conference on Concrete and Digital Fabrication; 2022. p. 37–42. https://doi.org/10.1007/978-3-031-06116-5_6.
[16] Langelaar M. Topology optimization of 3D self-supporting structures for additive manufacturing. Addit Manuf 2016;12:60–70. https://doi.org/10.1016/j.addma.2016.06.010.
[17] Liu J, Yu H. Concurrent deposition path planning and structural topology optimization for additive manufacturing. Rapid Prototyping J 2017;23:930–42. https://doi.org/10.1108/RPJ-05-2016-0087.
[18] Ma G, Li Z, Wang L, Wang F, Sanjayan J. Mechanical anisotropy of aligned fiber reinforced composite for extrusion-based 3D printing. Constr Build Mater 2019; 202:770–83. https://doi.org/10.1016/j.conbuildmat.2019.01.008.
[19] Misiun G, van de Ven E, Langelaar M, Geijselaers H, van Keulen F, van den Boogaard T, et al. Topology Optimization for additive manufacturing with distortion constraints. Comput Methods Appl Mech Eng 2021;386:114095. https://doi.org/10.1016/j.cma.2021.114095.
[20] Yamada T, Noguchi Y. Topology optimization with a closed cavity exclusion constraint for additive manufacturing based on the fictitious physical model approach. Addit Manuf 2022;52:102630. https://doi.org/10.1016/j.addma.2022.102630.
[21] Vantyghem G, De Corte W, Shakour E, Amir O. 3D printing of a post-tensioned concrete girder designed by topology optimization. Autom Constr 2020;112: 103084. https://doi.org/10.1016/j.autcon.2020.103084.
[22] Carstensen JV. Topology optimization with nozzle size restrictions for material extrusion-type additive manufacturing. Struct Multidiscip Optim 2020;62: 2481–97. https://doi.org/10.1007/s00158 -020-02620-5.
[23] Fernández E, Ayas C, Langelaar M, Duysinx P. Topology optimisation for large-scale additive manufacturing: generating designs tailored to the deposition nozzle size. Virtual Phys Prototyp 2021;16:196–220. https://doi.org/10.1080/17452759.2021.1914893.
[24] Pastore T, Menna C, Asprone D. Bézier-based biased random-key genetic algorithm to address printability constraints in the topology optimization of concrete structures. Struct Multidiscip Optim 2022;65:64. https://doi.org/10.1007/s00158-021-03119-3.
[25] Bi M, Tran P, Xia L, Ma G, Xie YM. Topology optimization for 3D concrete printing with various manufacturing constraints. Addit Manuf 2022;57:102982. https://doi.org/10.1016/j.addma.2022. 102982.
[26] Sigmund O. A 99 line topology optimization code written in Matlab. Struct Multidiscip Optim 2001;21:120–7. https://doi.org/10.1007/s001580050176.
[27] Andreassen E, Clausen A, Schevenels M, Lazarov BS, Sigmund O. Efficient topology optimization in MATLAB using 88 lines of code. Struct Multidiscip Optim 2011;43: 1–16. https://doi.org/10.1007/s00158-010-0594-7.
[28] Wang F, Lazarov BS, Sigmund O. On projection methods, convergence and robust formulations in topology optimization. Struct Multidiscip Optim 2010;43:767–84. https://doi.org/10.1007/s00158-010-0602-y.
[29] Huang X. Smooth topological design of structures using the floating projection. Eng Struct 2020;208:110330. https://doi.org/10.1016/j.engstruct.2020.110330.
[30] Li S, Sitnikova E, Liang Y, Kaddour A-S. The Tsai-Wu failure criterion rationalised in the context of UD composites. Compos Part A Appl Sci Manuf 2017;102:207–17. https://doi.org/10.1016/j.compositesa.2017.08.007.
[31] Tsai SW, Wu EM. A general theory of strength for anisotropic materials. J Compos Mater 1971;5:58–80. https://doi.org/10.1177/002199837100500106.
[32] Ma G, Yang W, Wang L. Strength-constrained simultaneous optimization of topology and fiber orientation of fiber-reinforced composite structures for additive manufacturing. Adv Struct Eng 2022;25:1636–51. https://doi.org/10.1177/13694332221088946.
[33] Svanberg K. The method of moving asymptotes—a new method for structural optimization. Int J Numer Meth Eng 1987;24:359–73. https://doi.org/10.1002/nme.1620240207.
[34] Zhang W, Zhong W, Guo X. An explicit length scale control approach in SIMP-based topology optimization. Comput Methods Appl Mech Eng 2014;282:71–86. https://doi.org/10.1016/j.cma.2014.08.027.
[35] Liu J. Piecewise length scale control for topology optimization with an irregular design domain. Comput Methods Appl Mech Eng 2019;351:744–65. https://doi.org/10.1016/j.cma.2019.04.014.
[36] Guo X, Zhang W, Zhong W. Explicit feature control in structural topology optimization via level set method. Comput Methods Appl Mech Eng 2014;272: 354–78. https://doi.org/10.1016/j.cma.2014.01.010.
[37] Xia Q, Shi T. Constraints of distance from boundary to skeleton: For the control of length scale in level set based structural topology optimization. Comput Methods Appl Mech Eng 2015;295:525–42. https://doi.org/10.1016/j.cma.2015.07.015.
[38] Yan X, Chen J, Hua H, Zhang Y, Huang X. Smooth topological design of structures with minimum length scale and chamfer/round controls. Comput Methods Appl Mech Eng 2021;383:113939. https://doi.org/10.1016/j.cma.2021.113939.
[39] Roul P, Prasad Goura VMK. B-spline collocation methods and their convergence for a class of nonlinear derivative dependent singular boundary value problems. Appl Math Comput 2019;341:428–50. https://doi.org/10.1016/j.amc.2018.09.011.

[40] Jin Y, He Y, Fu G, Zhang A, Du J. A non-retraction path planning approach for extrusion-based additive manufacturing. Robot Comput Integr Manuf 2017;48:132–44. https://doi.org/10.1016/j.rcim.2017.03.008.

[41] Ma G, Li Z, Wang L, Bai G. Micro-cable reinforced geopolymer composite for extrusion-based 3D printing. Mater Lett 2019;235:144–7. https://doi.org/10.1016/j.matlet.2018.09.159.

[42] Wang L, Liu Y, Yang Y, Li Y, Bai M. Bonding performance of 3D printing concrete with self-locking interfaces exposed to compression-shear and compression-splitting stresses. Addit Manuf 2021;42:101992. https://doi.org/10.1016/j.addma.2021.101992.